

FDTD Methods for 3-D Room Acoustics Simulation with High-order Accuracy in Space and Time

Brian Hamilton, *Member, IEEE* and Stefan Bilbao, *Senior Member, IEEE*

Abstract—Time-domain finite difference (FDTD) methods are popular tools for 3-D room acoustics modeling, but numerical dispersion is an inherent problem that can place limitations on the usable bandwidth of a given scheme. Compact explicit 27-point schemes and “large-star” schemes with high-order spatial differences offer improvements to the simplest scheme, but are ultimately limited by their second-order accuracy in time. In this paper, we use modified equation methods to derive FDTD schemes with high orders of accuracy in both space and time, resulting in significant improvements in numerical dispersion as compared to the aforementioned schemes. In comparison to such schemes, the high-order accurate schemes presented in this paper use significantly less memory and fewer operations when low error tolerances in numerical phase velocities are critical, leading to higher usable bandwidths for auralization purposes. Simulation results are also presented, demonstrating improved approximations to modal frequencies of a shoe-box room and free-space propagation of a bandlimited pulse.

Index Terms—Room acoustics, FDTD, finite difference methods, artificial reverberation.

I. INTRODUCTION

Wave-based methods such as time-domain finite difference (FDTD) methods [1]–[3] are becoming essential tools for room acoustics simulation, and have applications to artificial reverberation [4], sound source localization [5]–[7] and boundary impedance estimation [7], [8], as well as potential for use in virtual reality applications [9]. As opposed to conventional geometric methods like image source and ray-tracing methods (see, e.g., [10]), wave-based methods can capture all aspects of sound propagation in rooms, including full wave diffraction. Although wave-based methods come at a substantial computational cost in comparison to geometric methods, audio-rate simulations are becoming realizable through the use of modern graphics processing units (GPU) devices [11]–[13]. Other wave-based methods include boundary element [14] and finite element [15] methods, although FDTD is often preferred due to its ease of implementation and parallelization. Hybridizations of wave and geometric methods have also been studied [16], [17].

An important problem in the study of FDTD methods is the presence of numerical dispersion, as it places limits on the usable bandwidth reproduced by a scheme due to mistunings of modes and incorrect modal densities [3], and/or

audible phase artifacts [18]. Mitigating such effects through grid oversampling incurs significant additional computational costs and therefore is not always practical for large-scale simulations. To that end, there has been much work in the area of reducing numerical dispersion in 3-D schemes—e.g., through the use of closely-related digital waveguide mesh (DWM) topologies [19], [20] and with 27-point compact explicit FDTD schemes [3]. Recently, two-step explicit “large-star” schemes employing high-order spatial differencing [21], yet remaining second-order accurate in time, have been proposed as viable alternatives to second-order accurate 27-point compact explicit schemes [3]. Implicit schemes with fourth-order accuracy in both space and time have also been considered [22], [23], but linear system solutions required at each time-step may be prohibitively expensive [23]. Two-step explicit FDTD schemes with high orders of accuracy in both space and time have yet to be considered in the context of 3-D room acoustics simulation.

The main contribution of this paper is to present a set of two-step explicit schemes that display high orders of accuracy in time and space for the 3-D wave equation, derived through the use of modified equation methods. Numerical dispersion analyses are carried out to demonstrate that these schemes offer significant improvements in terms of computational costs required to achieve low error thresholds in numerical phase velocities over a given range of frequencies, as compared to the aforementioned explicit schemes. Simulation results are also presented in order to verify that these schemes perform better than compact explicit and large-star schemes, and thus warrant further investigation towards the ultimate goal of large-scale 3-D room acoustics simulations over non-trivial domains with frequency-dependent impedance boundary terminations.

The organization of this paper is as follows. In Section II, we review the basics of finite difference schemes for the wave equation and 27-point compact explicit schemes [3]. In Section III, we review high-order-in-space schemes (as considered in [21]) and provide additional insights into their numerical dispersion and orders of accuracy. In Section IV, we present our high-order accurate schemes derived using modified equation methods. In Section V we compare the various schemes in terms of numerical dispersion and computational efficiency, and in Section VI we present simulation results.

II. BACKGROUND

A. Model Equations

The starting model for 3-D room acoustics simulation is the 3-D wave equation, which can be expressed as:

$$(\partial_t^2 - c^2 \Delta) u = 0. \quad (1)$$

Manuscript received XXXXX XX, 2017; revised XXXXX XX, 2017; accepted XXXXX XX, 2017. Date of publication XXXXX XX, 2017; date of current version XXXXX XX, 2017. This work was supported by the European Research Council under Grants StG-2011-279068-NESS and PoC-2016-737574-WRAM. The associate editor coordinating the review of this manuscript and approving it for publication was Prof. Firstname Lastname.

The authors are with the Acoustics and Audio Group, University of Edinburgh, UK (e-mail: brian.hamilton@ed.ac.uk).

Digital Object Identifier 10.1109/TASLP.2017.00000000

Here, $u = u(t, \mathbf{x})$ is a scalar field, which could represent an acoustic velocity potential or sound pressure field [24], $t \geq 0$ is time in seconds, $\mathbf{x} = (x, y, z) \in \mathbb{R}^3$ is a spatial position in 3-D (coordinates x, y, z in m), and c is the speed of sound in air (taken to be a constant; e.g., $c = 340$ m/s). The notation ∂_t denotes a partial derivative with respect to time, $\Delta = \partial_x^2 + \partial_y^2 + \partial_z^2$ is the 3-D Laplacian, and ∂_w denotes a partial derivative with respect to the spatial coordinate w , which throughout the paper will represent any coordinate direction in \mathbb{R}^3 ; i.e., $w \in \{x, y, z\}$. Required initial conditions are $u(0, \mathbf{x})$ and $\partial_t u(t, \mathbf{x})|_{t=0}$. It is worth recalling that solutions of the wave equation are generally not known in analytic forms (apart from some special cases), hence numerical methods like FDTD must be employed.

In the frequency-domain, the wave equation is represented by its dispersion relation, which can be derived by considering a plane-wave trial solution of the form $u = \exp(j(\omega t + \mathbf{k} \cdot \mathbf{x}))$, where $j = \sqrt{-1}$, $\omega \in \mathbb{R}$ is a temporal angular frequency in rad/s and $\mathbf{k} = (k_x, k_y, k_z) \in \mathbb{R}^3$ the wave vector (with $k = |\mathbf{k}|$ the wavenumber in rad/m). The dispersion relation and phase velocity for the wave equation are then found to be, respectively:

$$\omega = \pm c|\mathbf{k}| \implies v_p := \frac{\omega}{|\mathbf{k}|} = \pm c, \quad (2)$$

which simply states that plane waves travel with the speed c regardless of their frequency.

The wave equation can be augmented with viscothermal and/or relaxation effects for a more complete description of sound propagation in air, but such effects, which lead to dissipation in high frequencies, can be neglected for the purposes of this study; see, e.g., [25], [26]. Of course, for the simulation of realistic room acoustics, the wave equation must also be accompanied by suitable boundary conditions to model reflection and absorption from wall materials. While a full room acoustics problem (i.e., including impedance boundary conditions over complex geometries, as in, e.g., [27]) is the eventual goal, this study will only be concerned with improving the approximation of sound propagation throughout the interior of a room, which is the bulk of the computation in any FDTD room acoustics simulation. However, as a first step towards the full boundary problem, boundary conditions for a rigid cuboid room will be implemented, and the topic of more complex boundary truncation will be left as future work (discussed further in Section VII). Sources and methods for spatialized outputs will also be neglected in this work (see, e.g., [28]–[31]).

B. Shift and difference operators, and discrete Laplacians

In order to discretize the 3-D wave equation with Cartesian grid-based FDTD schemes, let $u_l^n \approx u(nT, lX)$ represent an approximation to $u(t, \mathbf{x})$ at time $t = nT$, $n \in \mathbb{Z}$, $n \geq 0$ and position $\mathbf{x} = lX$, $l = (l_x, l_y, l_z) \in \mathbb{Z}^3$, where X is the Cartesian grid spacing and T is the time-step. $F_s = 1/T$ is the sample rate in Hz. Next, we introduce shift operators acting on u_l^n :

$$e_{t\pm} u_l^n := u_l^{n\pm 1}, \quad e_{w\pm} u_l^n := u_{l\pm \hat{e}_w}^n, \quad (3)$$

where \hat{e}_w are the standard unit vectors in \mathbb{R}^3 . The notation $u_{l\pm \hat{e}_w}^n$ is chosen for convenience, but for implementation

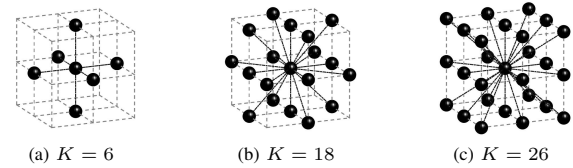


Fig. 1: Various $(K+1)$ -point stencils on the 3-D Cartesian grid used in by $\delta_{\Delta,26}$ (defined by (8)), with K as indicated.

purposes it helps to know that:

$$u_{l\pm \hat{e}_x}^n = u_{l_x \pm 1, l_y, l_z}^n, \quad u_{l\pm \hat{e}_y}^n = u_{l_x, l_y \pm 1, l_z}^n, \quad u_{l\pm \hat{e}_z}^n = u_{l_x, l_y, l_z \pm 1}^n. \quad (4)$$

We can then define temporal and spatial difference operators:

$$\delta_{tt} := \frac{1}{T^2}(e_{t+} - 2 + e_{t-}) = \partial_t^2 + \mathcal{O}(T^2), \quad (5a)$$

$$\delta_{ww} := \frac{1}{X^2}(e_{w+} - 2 + e_{w-}) = \partial_w^2 + \mathcal{O}(X^2). \quad (5b)$$

Note that the above operators are second-order accurate in time and space, respectively. Also, it will be convenient throughout this paper to use the following shorthand notation:

$$\delta_w^2 := X^2 \delta_{ww}. \quad (6)$$

With the above, we can define a general discrete Laplacian as:

$$\delta_{\Delta} = \frac{1}{X^2} [\delta_x^2 + \delta_y^2 + \delta_z^2 + \Phi(\delta_x^2, \delta_y^2, \delta_z^2)], \quad (7)$$

where Φ represents any trinomial in $\delta_x^2, \delta_y^2, \delta_z^2$ such that $\Phi = \mathcal{O}(X^{2M})$ with $M \geq 2$, or $\Phi = 0$. Given these constraints, any such discrete Laplacian has at least second-order accuracy in space; i.e., we can write $\delta_{\Delta} = \Delta + \mathcal{O}(X^2)$.

We say that such a discrete Laplacian uses a $(K+1)$ -point stencil,¹ where K is the number of neighboring points accessed on the Cartesian grid. For example, a well-known family of schemes [3], [32] uses the following special case with $K \leq 26$:

$$\delta_{\Delta,26} := \frac{1}{X^2} [\delta_x^2 + \delta_y^2 + \delta_z^2 + a(\delta_x^2 \delta_y^2 + \delta_y^2 \delta_z^2 + \delta_x^2 \delta_z^2) + b\delta_x^2 \delta_y^2 \delta_z^2], \quad (8)$$

where $a, b \in \mathbb{R}$ are free parameters. Example stencil configurations for $\delta_{\Delta,26}$ are shown in Fig. 1.

C. Two-step explicit Cartesian schemes

The schemes to be considered throughout this paper, and indeed many of the schemes that have been analyzed in previous work (e.g., [3], [32], [33]), can be written in the form of a general two-step explicit scheme:

$$(\delta_{tt} - c^2 \delta_{\Delta}) u_l^n = 0, \quad (9)$$

where the particular form of δ_{Δ} will be specified for each scheme under consideration. For example, the choice of $\delta_{\Delta} = \delta_{\Delta,26}$ leads to the so-called “compact explicit” schemes [3].

Any scheme of the above form can be rewritten as an explicit two-step recursion:

$$u_l^{n+1} = (2 + c^2 T^2 \delta_{\Delta}) u_l^n - u_l^{n-1}, \quad (10)$$

¹In this work we use the term “stencil” to describe the set of points that contribute in a discrete Laplacian δ_{Δ} . This usage differs from a recent article [21], where “stencil” is employed to describe what we call a “scheme”.

where only two states need to be stored in memory since u_l^{n+1} can overwrite u_l^{n-1} in place. Each pointwise update in space may be carried out in parallel, requiring $K + 1$ floating-point instructions when fused-multiply-add operations are available, such as on modern GPUs [34]. As we are considering three spatial dimensions, the memory required to simulate a given volume scales with X^{-3} .

The simplest scheme for the 3-D wave equation [35], also known as *standard rectilinear* [2], [36], [37] and *standard leapfrog* (SLF) [3] has the form (9) with $\delta_\Delta = \delta_{\Delta,26}|_{a=b=0}$ (with a seven-point stencil illustrated by Fig. 1(a)) and the following two-step update:

$$u_l^{n+1} = \lambda^2 (u_{l+\hat{e}_x}^n + u_{l+\hat{e}_y}^n + u_{l+\hat{e}_z}^n + u_{l-\hat{e}_x}^n + u_{l-\hat{e}_y}^n + u_{l-\hat{e}_z}^n) + (2 - 6\lambda^2)u_l^n - u_l^{n-1}, \quad (11)$$

where $\lambda := cT/X > 0$ is known as the Courant number. Two other important special cases are the “ISO” (short for “isotropic”) scheme $\delta_\Delta = \delta_{\Delta,26}|_{a=1/6, b=0}$ [3], whose 19-point stencil is shown in Fig. 1(b); and the so-called “interpolated wideband” (IWB) scheme with $\delta_\Delta = \delta_{\Delta,26}|_{a=1/4, b=1/16}$ [3], whose 27-point stencil is shown in Fig. 1(c).

D. Numerical stability

Numerical stability is critical to the practical use of finite difference schemes. In the free-space case, conditions for numerical stability can be determined using von Neumann analysis [38]. For this we consider a discrete plane-wave ansatz of the form $u_l^n = \exp(j(n\omega_T + \mathbf{l} \cdot \mathbf{k}_X))$, where $\omega_T := \omega T \in [-\pi, \pi]$ is a normalized frequency and $\mathbf{k}_X := \mathbf{k}X \in [-\pi, \pi]^3$ is a normalized wave vector ($k_X := |\mathbf{k}_X|$ is the normalized wavenumber); for such solutions, the operators δ_{tt} and δ_{ww} behave as follows:

$$\delta_{tt}u_l^n = -\frac{4}{T^2}\hat{s}_t u_l^n, \quad \delta_{ww}u_l^n = -\frac{4}{X^2}\hat{s}_w u_l^n, \quad (12)$$

where $\hat{s}_t := \sin^2(\omega_T/2)$, and $\hat{s}_w := \sin^2(\mathbf{k}_X \cdot \hat{\mathbf{e}}_w/2)$. In other words, \hat{s}_t and \hat{s}_w are the *Fourier symbols* of $-\frac{T^2}{4}\delta_{tt}$ and $-\frac{X^2}{4}\delta_{ww}$, respectively. A frequency-domain representation of the general scheme (9) is then:

$$\hat{s}_t = \lambda^2 F, \quad (13)$$

where $F = F(\mathbf{k}_X)$ is the symbol of $-\frac{X^2}{4}\delta_\Delta$ (e.g., $F = \hat{s}_x + \hat{s}_y + \hat{s}_z$ for the SLF scheme), and F may also contain real-valued free parameters.

Provided that \hat{s}_t is non-negative and bounded by unity, plane-waves will propagate in this scheme without loss and without exponential growth (von Neumann stability [35], [39]). This leads to the following conditions for numerical stability:

$$0 \leq \lambda^2 F \leq 1. \quad (14)$$

These conditions hold for any scheme whose frequency-domain form is (13) with F real-valued. If the term Φ in (7) is independent of the Courant number, then (14) simplifies to:

$$F \geq 0, \quad \lambda \leq \lambda_{\max} := \sqrt{\max_{\mathbf{k}_X} F}. \quad (15)$$

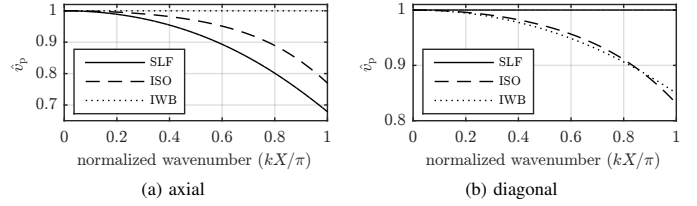


Fig. 2: Relative phase velocities for SLF, ISO, and IWB schemes with $\lambda = \lambda_{\max}$, for wavenumbers $kX \leq \pi$ along (a): axial direction ($k_x \neq 0, k_y = k_z = 0$) and (b): diagonal direction ($k_x = k_y = k_z$).

For example, under the family of compact explicit schemes of [3], [32] (i.e., with $\delta_\Delta = \delta_{\Delta,26}$), we have for the function F :

$$F = \hat{s}_x + \hat{s}_y + \hat{s}_z - 4a(\hat{s}_x\hat{s}_y + \hat{s}_y\hat{s}_z + \hat{s}_x\hat{s}_z) + 16b\hat{s}_x\hat{s}_y\hat{s}_z. \quad (16)$$

The above function is multilinear in \hat{s}_w terms, so the extrema are found at $\hat{s}_w \in \{0, \pi\}$, meaning that the condition $F \geq 0$ can be simplified to [3], [32]:

$$a \leq 1/2, \quad b \geq (12a - 3)/16, \quad (17)$$

while $\lambda^2 F \leq 1$ can be rewritten as:

$$\lambda \leq \lambda_{\max} = (\max[1, (2 - 4a), (3 - 12a + 16b)])^{-1/2}. \quad (18)$$

For the simplest scheme ($a = b = 0$), $\lambda_{\max} = \sqrt{1/3}$; for the ISO scheme ($a = 1/6, b = 0$), $\lambda_{\max} = \sqrt{3/4}$; and for the IWB scheme ($a = 1/4, b = 1/16$), $\lambda_{\max} = 1$. It is generally best to choose λ as high as possible, as this minimizes the number of time-steps to be computed for a given grid resolution, and leads to optimal dispersion in many schemes (see, e.g., [3]).

E. Numerical dispersion and numerical phase velocities

The dispersion relation of the numerical scheme—an approximation to that of the wave equation (in (2))—is essentially Eq. (13), but we can rewrite it more precisely as:

$$\omega_T(\mathbf{k}_X) = 2 \arcsin \left(\pm \lambda \sqrt{F(\mathbf{k}_X)} \right). \quad (19)$$

By symmetry, we will consider only $\omega_T \geq 0$ and $\mathbf{k}_X \in [0, \pi]^3$ for the remainder of this study. The dispersion relation is generally non-linear and consequently, temporal frequencies experience a warping effect, leading to a mistuning of modes in an enclosed space.

A numerical phase velocity may also be defined as:

$$\hat{v}_p(\mathbf{k}_X) := \frac{\omega_T(\mathbf{k}_X)}{\lambda |\mathbf{k}_X|}. \quad (20)$$

This describes the relative speed at which plane-wave components travel in a given scheme, which is ideally unity. For any consistent (and stable) FDTD scheme $\hat{v}_p \rightarrow 1$ as $k_X \rightarrow 0$, which, in turn, means that $|1 - \hat{v}_p|$ tends to increase with the wavenumber. For example, Fig. 2 shows the relative phase velocity for SLF, ISO, and IWB schemes, for $k_X \in [0, \pi]$ along axial and diagonal directions,² which tend to be the

²We should note that we only consider wavenumbers up to $k_X = \pi$, because this is the spatial bandlimit on the Cartesian grid for representing a signal isotropically (i.e., independent of direction) [40], and because $k_X = \pi$ is associated to a *transition frequency* above which modal densities tend to be incorrect in an enclosed domain [41].

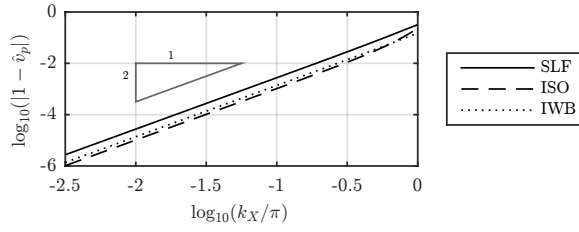


Fig. 3: Relative dispersion error as a function of wavenumber along worst-case directions for SLF, ISO, and IWB schemes.

extreme-case directions in Cartesian grid-based schemes [3]. We see that apart from diagonal and axial directions for SLF and IWB schemes, respectively, deviations from unity can be significant in upper portions of the simulated bandwidth—at $k_X = \pi$ phase velocity errors reach 33%, 23%, and 15%, respectively for the SLF, ISO, and IWB schemes.

F. Order of accuracy

The order of accuracy (OoA) is an important characteristic of a scheme, and a central theme of this study. Formally, the OoA of a fully-discrete numerical scheme is defined as the minimum rate at which the numerical solution converges to an exact solution under refinement of both T and X , usually while keeping the grid ratio fixed to some value [38]. Provided that the scheme is stable, the OoA of the scheme is revealed by its truncation error by the Lax equivalence theorem [38].

For the two-step schemes considered in this study, we have the following Taylor expansion:

$$\delta_{tt} - c^2 \delta_{\Delta} = \partial_t^2 - c^2 \Delta + \text{T.E.}, \quad (21)$$

where the term denoted “T.E.” represents the truncation error of the scheme. Then, for a scheme with $2M$ th-order accuracy ($M \geq 1$), one can expect that:

$$\text{T.E.} = \mathcal{O}(X^{2M}) = \mathcal{O}(T^{2M}), \quad (22)$$

where the latter “equality” above results from the fact that λ is fixed and $X = cT/\lambda$. It is important to note that the use of centered operators (e.g., δ_{tt} and δ_{ww}) tends to lead to even-order accuracy; hence, in this paper $M = 2$ implies fourth-order accuracy, and so on. Typically, for a scheme to be called “high(er)-order accurate” it must have an OoA higher than two (i.e., $M > 1$ for even-order accuracy).

It is also important to note that the OoA of a scheme is not only determined by the individual operators in the scheme, but also the balance of their respective temporal and spatial errors, which may cancel, meaning that second-order operators can possibly lead to high-order accuracy. The most notable example of this is the *digital waveguide* algorithm [42], or more generally, the simplest FDTD scheme in 1-D [43], which is able to achieve infinite order accuracy by employing only the second-order accurate finite difference operators δ_{tt} and δ_{xx} (see, e.g., [44, Section 6.2.4]).

It can also be shown that the OoA of a scheme is reflected in its relative dispersion error. Since the scheme is itself defined by the equation (9), we can say that such a scheme with $2M$ th-order accuracy would satisfy the equation:

$$\partial_t^2 - c^2 \Delta = \mathcal{O}(X^{2M}). \quad (23)$$

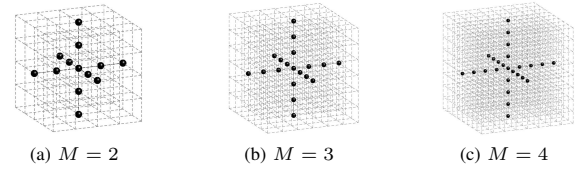


Fig. 4: $(6M + 1)$ -point stencils on the 3-D Cartesian grid. The case $M = 1$ is illustrated in Fig. 1(a).

In the case of plane-wave solutions, the above transforms to:

$$-\omega^2 + c^2 |\mathbf{k}|^2 = \mathcal{O}(X^{2M}), \quad (24)$$

where ω and \mathbf{k} are still related through (19). Dividing through by $c^2 |\mathbf{k}|^2$, the above can be rewritten as:

$$\hat{v}_p^2 = 1 - \mathcal{O}(X^{2M}), \quad (25)$$

Finally, we take the square root of both sides and in the limit of small X we have $\sqrt{1 - \mathcal{O}(X^{2M})} \approx 1 - \mathcal{O}(X^{2M})$, allowing us to write:

$$1 - \hat{v}_p = \mathcal{O}(X^{2M}). \quad (26)$$

Thus, if we plot $\log(|1 - \hat{v}_p|)$ with respect to $\log(k_X)$ in a $2M$ th-order accurate scheme, we should see a negative slope of $2M$ as k_X approaches zero—at least along any non-exact direction. As an example, we plot this in Fig. 3 for the SLF, ISO, and IWB schemes. Indeed, we observe a negative slope of two along respective worst-case directions, reflecting the fact that these schemes are second-order accurate (i.e., they have an OoA of two ($M = 1$)).

III. SCHEMES WITH HIGH-ORDER SPATIAL DIFFERENCING

Recently, a family of two-step explicit “large-star” schemes were proposed as alternatives to the SLF and IWB schemes [21]. Such schemes—which have a long history in the field of geophysics [45]–[47]—employ $(6M + 1)$ -point stencils that reach out to M neighboring points along each coordinate direction, as illustrated in Fig. 4, in order to achieve a high order of accuracy in space (combined with a second-order accuracy in time).

While such schemes are sometimes referred to as “higher-order accurate schemes” (e.g., in [21])—in reference to the underlying high-order approximation to the Laplacian—one should not conflate the concept of spatial accuracy with the global accuracy of the scheme (i.e., with respect to the wave equation itself). The purpose of this section is to elaborate on this point, through an analysis of the numerical dispersion of these schemes, using the concepts introduced in Section II.

The key component of the large-star schemes is a family of high-order accurate, centered second-order finite difference operators, which we can write as:

$$\delta_{ww}^{(M)} := \sum_{m=-M}^M \frac{a_{M,m}}{X^2} e_{w+}^m = \partial_w^2 + \mathcal{O}(X^{2M}), \quad (27)$$

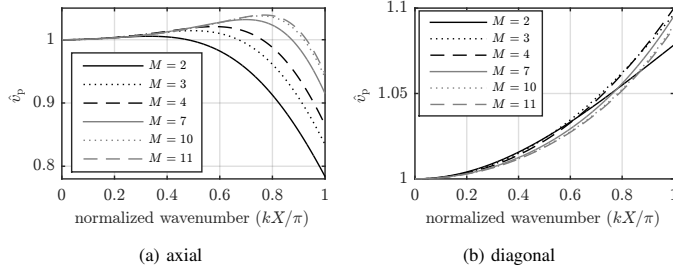


Fig. 5: Relative phase velocities for $2M$ th-order-in-space $(6M+1)$ -point schemes with M as indicated and $\lambda = \lambda_{\max, M}$, for wavenumbers $k_X \leq \pi$ along (a) axial and (b) diagonal directions.

where $e_{w+}^m := (e_{w+})^m$ and $e_{w+}^{-m} := e_{w-}^m$, and where the coefficients $a_{M,m}$ are given by:

$$a_{M,m} = \frac{2(-1)^{m-1}(M!)^2}{m^2(M-m)!(M+m)!}, \quad m = 1, \dots, M \quad (28a)$$

$$a_{M,0} = -2 \sum_{m=1}^M a_{M,m}, \quad a_{M,-m} = a_{M,m}. \quad (28b)$$

These coefficients were individually derived in [21] up to $M = 8$, but they are completely determined by the general formula above (derived in [46]). It follows that we can construct a discrete Laplacian with $2M$ th-order accuracy as:

$$\delta_{\Delta}^{(M)} := \delta_{xx}^{(M)} + \delta_{yy}^{(M)} + \delta_{zz}^{(M)} = \Delta + \mathcal{O}(X^{2M}). \quad (29)$$

The two-step explicit schemes analyzed in [21] can then be expressed by (9) or (10) with $\delta_{\Delta} = \delta_{\Delta}^{(M)}$. Note that the case of $M = 1$ gives the SLF scheme (i.e., $\delta_{\Delta}^{(1)} = \delta_{\Delta,26}|_{a=b=0}$).

It is also worth noting that an equivalent representation of $\delta_{ww}^{(M)}$ [48] is:

$$\delta_{ww}^{(M)} = \sum_{m=1}^M \frac{b_m}{X^2} \delta_w^{2m}, \quad b_m = \frac{2(-1)^{m-1}((m-1)!)^2}{(2m)!}, \quad (30)$$

where $\delta_w^{2m} := (\delta_w^2)^m$ and $m \geq 1$. Although not featured in [21], the above representation is particularly useful for the analysis of numerical stability.

A. Numerical stability analysis

Towards a numerical stability condition, as a first attempt we may insert the plane-wave ansatz into the scheme, from which we obtain a relation of the form (13) with:

$$F = F_M := \sum_{m=1}^M a_{M,m} (\hat{s}_{x,m} + \hat{s}_{y,m} + \hat{s}_{z,m}), \quad (31)$$

where $\hat{s}_{w,m} := \sin^2(\mathbf{k} \cdot \hat{\mathbf{e}}_w mX/2)$ (and $\hat{s}_{w,1} = \hat{s}_w$), and F_M can be seen as the Fourier transform of $-\frac{X^2}{4}\delta_{\Delta}^{(M)}$. However, the conditions (14) are not easily verified in general (for $M > 1$) from the above representation, since $a_{M,m}$ alternates in sign while each term $\hat{s}_{w,m}$ is positive. In particular, we cannot immediately ascertain the non-negativity of F_M for $M > 1$, nor can we easily determine its maximal values. On the other

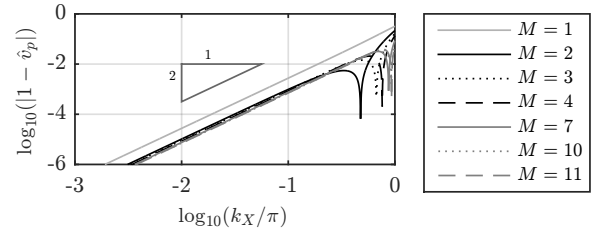


Fig. 6: Relative dispersion error as a function of wavenumber along axial directions for various $2M$ th-order-in-space schemes with $\lambda = \lambda_{\max, M}$. In this logarithmic plot, a negative slope of two is observed as k_X approaches zero for all $M \geq 1$, reflecting a second-order accuracy with respect to the wave equation.

hand, using (30), we also have that [46]:

$$F_M = \sum_{m=1}^M \gamma_m (\hat{s}_x^m + \hat{s}_y^m + \hat{s}_z^m), \quad \gamma_m = \frac{2^{2m-1}((m-1)!)^2}{(2m)!}, \quad (32)$$

where $\hat{s}_w^m = (\hat{s}_w)^m$. From the above we can easily see that $F_M \geq 0$. Furthermore, it is clear that F_M increases monotonically for $k_X \in [0, \pi]$ along axial directions, meaning that extrema appear at $k = 0$ and $k_x = k_y = k_z = \pi/X$. After [46], a general stability condition (not reported in [21]) is then found to be $\lambda \leq \lambda_{\max, M}$, where:

$$\lambda_{\max, M} := (3\Upsilon_M)^{-1/2}, \quad \Upsilon_M := \sum_{m=1}^M \gamma_m = \sum_{\substack{1 \leq m \leq M, \\ m \text{ odd}}} a_{M,m}. \quad (33)$$

For example, $\lambda_{\max, 2} = 0.5$ and $\lambda_{\max, 3} = \sqrt{15/68} \approx 0.469$. Also, it has been shown that $\lim_{M \rightarrow \infty} \Upsilon_M^{-1} = 2/\pi$ [46]—a limiting value that was conjectured to be equal to $1/2$ in [21, Section III.A]—meaning that these stability limits converge to the value $\lambda_{\max, \infty} = \sqrt{2/(3\pi)}$.

B. On high-order accuracy

At this point we can discuss and analyze the OoA of the large-star schemes. For this family of schemes, we have the Taylor expansion:

$$\delta_{tt} - c^2 \delta_{\Delta}^{(M)} = \partial_t^2 - c^2 \Delta + \text{T.E.}, \quad (34)$$

where T.E., the truncation error, is:

$$\text{T.E.} = \mathcal{O}(T^2) + \mathcal{O}(X^{2M}). \quad (35)$$

For λ fixed (e.g., to $\lambda = \lambda_{\max, M}$ as in [21]) and c fixed, we can make the substitution $T = X\lambda/c$, which implies that:

$$\text{T.E.} = \mathcal{O}(T^2) + \mathcal{O}(X^{2M}) = \mathcal{O}(X^2) = \mathcal{O}(T^2). \quad (36)$$

This simply shows that the second-order temporal error dominates in the limit of small grid spacings (or high sample rates for λ fixed), and consequently, these schemes have a second-order rate of convergence with respect to X or T (keeping λ, c fixed). In other words, we find that these schemes are only second-order accurate for the wave equation, for all $M \geq 1$, despite the higher-order accurate approximation to the underlying Laplacian operator. As such, they cannot be said to be “high-order accurate” for the wave equation, in the strict

sense at least. Indeed, analyzing the error in the relative phase velocity in Fig. 6, we see that these schemes converge towards the ideal dispersion relation with $\mathcal{O}(X^2)$ for all $M \geq 1$.

IV. HIGH-ORDER ACCURATE SCHEMES

Having seen that the large-star schemes are in fact only second-order accurate for the wave equation, it remains to derive and explore two-step schemes with high-order accuracy—i.e., with orders of accuracy greater than two. Towards that goal, in this section we investigate the use of stencils that reach out to axial and non-axial neighboring points, with stencil weights carefully set according to linear constraints obtained through operator expansions and modified equation methods [47], [49], [50], following previous work for 2-D schemes from the current authors [51], [52].

The family of schemes under consideration in this section can be written in the general form (9), using the following $(K+1)$ -point discrete Laplacian with $K \leq 62$:

$$\begin{aligned} \delta_{\Delta,62} := & \frac{1}{X^2} \left[a_1 (\delta_x^2 + \delta_y^2 + \delta_z^2) + a_2 (\delta_x^2 \delta_y^2 + \delta_y^2 \delta_z^2 + \delta_x^2 \delta_z^2) \right. \\ & + a_3 (\delta_x^4 + \delta_y^4 + \delta_z^4) + a_4 (\delta_x^2 \delta_y^2 \delta_z^2) + a_6 (\delta_x^6 + \delta_y^6 + \delta_z^6) \\ & \left. + a_5 (\delta_x^4 \delta_y^2 + \delta_x^2 \delta_y^4 + \delta_y^4 \delta_z^2 + \delta_y^2 \delta_z^4 + \delta_x^4 \delta_z^2 + \delta_x^2 \delta_z^4) \right]. \quad (37) \end{aligned}$$

Here, a_1, \dots, a_6 are real-valued free parameters and $a_1 \equiv 1$ is required for consistency. Expanding products of difference operators and collecting terms, the two-step update equation for this family of schemes can be compactly expressed by:

$$u_l^{n+1} = -u_l^{n-1} + \sum_{q_x=0}^3 \sum_{q_y=0}^{3-q_x} \sum_{q_z=0}^{3-q_x-q_y} d_{q_x q_y q_z} u_{l_x+q_x, l_y+q_y, l_z+q_z}^n, \quad (38)$$

where

$$\begin{aligned} d_{100} &= \lambda^2 \alpha_1, & d_{110} &= \lambda^2 \alpha_2 / 4, & d_{200} &= \lambda^2 \alpha_3 / 4, \\ d_{111} &= \lambda^2 \alpha_4 / 4, & d_{210} &= \lambda^2 \alpha_5 / 20, & d_{300} &= \lambda^2 \alpha_6 / 9, \\ d_{000} &= 2 - (6d_{100} + 12d_{110} + 6d_{200} + 8d_{111} + 24d_{210} + 6d_{300}), \end{aligned} \quad (39)$$

and $d_{q_x q_y q_z} = d_{q_x q_z q_y} = d_{q_y q_x q_z} = d_{q_y q_z q_x} = d_{q_z q_x q_y} = d_{q_z q_y q_x}$. The parameters $\alpha_1, \dots, \alpha_6$ appearing above can be related to the parameters a_1, \dots, a_6 appearing in (37) through the following linear system:

$$\begin{pmatrix} \alpha_1 \\ \alpha_2 \\ \alpha_3 \\ \alpha_4 \\ \alpha_5 \\ \alpha_6 \end{pmatrix} = \begin{pmatrix} 1 & -4 & -4 & 4 & 28 & 15 \\ 0 & 4 & 0 & -8 & -32 & 0 \\ 0 & 0 & 4 & 0 & -16 & -24 \\ 0 & 0 & 0 & 4 & 0 & 0 \\ 0 & 0 & 0 & 0 & 20 & 0 \\ 0 & 0 & 0 & 0 & 0 & 9 \end{pmatrix} \begin{pmatrix} a_1 \\ a_2 \\ a_3 \\ a_4 \\ a_5 \\ a_6 \end{pmatrix}. \quad (40)$$

This parametrized discrete Laplacian can also be seen as the linear combination of six distinct discrete Laplacians, each second-order accurate (following [41]) and weighted by elements of the column-vector $\alpha := (\alpha_1, \dots, \alpha_6)^T$. Using α , the condition for consistency can also be written as $\mathbf{1} \cdot \alpha = 1$, where $\mathbf{1}$ is a column-vector of ones. Note that for $a_3 = a_5 = a_6 = 0$, the compact explicit schemes considered in Section II are recovered (with $a = a_2$ and $b = a_4$). This family

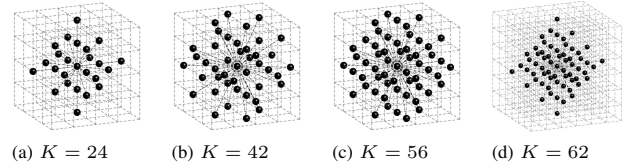


Fig. 7: Various $(K+1)$ -point stencils for the discrete Laplacian $\delta_{\Delta,62}$ on the 3-D Cartesian grid, with K as indicated. Stencil (a) results when $\alpha_1, \alpha_2, \alpha_3 \neq 0$ and $\alpha_4 = \alpha_5 = \alpha_6 = 0$. Stencil (b) results when $\alpha_1, \alpha_2, \alpha_5 \neq 0$ and $\alpha_3 = \alpha_4 = \alpha_6 = 0$. Stencil (c) results when $\alpha_1, \dots, \alpha_5 \neq 0$ and $\alpha_6 = 0$. Stencil (d) results when $\alpha_1, \dots, \alpha_6 \neq 0$.

also comprises the large-star schemes for $M \leq 3$. There are obviously many other stencil configurations possible depending on the non-zero elements of α ; see Fig. 7 for some special cases to be considered shortly. For plane-wave analyses, the scheme (38) transforms to (13) with:

$$\begin{aligned} F = & a_1 (\hat{s}_x + \hat{s}_y + \hat{s}_z) - 4a_2 (\hat{s}_x \hat{s}_y + \hat{s}_y \hat{s}_z + \hat{s}_x \hat{s}_z) \\ & - 4a_3 (\hat{s}_x^2 + \hat{s}_y^2 + \hat{s}_z^2) + 16a_4 (\hat{s}_x \hat{s}_y \hat{s}_z) + 16a_6 (\hat{s}_x^3 + \hat{s}_y^3 + \hat{s}_z^3) \\ & + 16a_5 (\hat{s}_x^2 \hat{s}_y + \hat{s}_x \hat{s}_y^2 + \hat{s}_y^2 \hat{s}_z + \hat{s}_y \hat{s}_z^2 + \hat{s}_x^2 \hat{s}_z + \hat{s}_x \hat{s}_z^2). \quad (41) \end{aligned}$$

A. Deriving high-order accuracy via modified equations

The process by which we derive high-order accurate schemes follows previous work using modified equation methods³ for 2-D schemes [51], [52], and for this family of schemes we limit our attention to fourth- and sixth-order accuracy. It is important to point out that with this approach, one does not proceed by specifying high-order accuracy in time and/or space separately. Rather, the goal is a delicate balance of spatial and temporal errors such that they effectively cancel to some high order. The first step is to constrain our schemes for fourth- and sixth-order isotropy in the discrete Laplacian, then we impose constraints for fourth- and sixth-order accuracy.

1) *Isotropy*: Since we aim to cancel spatial errors with temporal errors—which themselves are independent of spatial direction—we must ensure that spatial errors have some degree of isotropy [51]. Isotropy up to $2M$ th-order (i.e., “ $2M$ th-order isotropy”) in a discrete Laplacian δ_{Δ} means that we can write:

$$\delta_{\Delta} = \Delta + \sum_{m=1}^{M-1} C_m X^{2m} \Delta^m + \mathcal{O}(X^{2M}), \quad (42)$$

for dimensionless C_m , which may be affine functions of any free parameters in δ_{Δ} .

In order to write our discrete Laplacian $\delta_{\Delta,62}$ in the above form, we first consider the case of fourth-order isotropy ($M = 2$ in (42)). Expanding $\delta_{\Delta,62}$ in a Taylor series to fourth-order in X , we have:

$$\begin{aligned} \delta_{\Delta,62} = & \Delta + \frac{X^2}{60} \left[((5, 5, 20, 5, 17, 45) \cdot \alpha) (\partial_x^4 + \partial_y^4 + \partial_z^4) \right. \\ & \left. + ((0, 15, 0, 30, 24, 0) \cdot \alpha) (\partial_x^2 \partial_y^2 + \partial_x^2 \partial_z^2 + \partial_y^2 \partial_z^2) \right] + \mathcal{O}(X^4), \end{aligned} \quad (43)$$

³In the context of FDTD methods, a “modified equation” is the partial differential equation that is solved exactly by the FDTD scheme, usually obtained through Taylor expansion of the scheme, and “modified equation methods” is a general term that comprises manipulations of such expansions [47].

and we know that the biharmonic operator (Δ^2) may be expanded as

$$\Delta^2 = \partial_x^4 + \partial_y^4 + \partial_z^4 + 2(\partial_x^2 \partial_y^2 + \partial_x^2 \partial_z^2 + \partial_y^2 \partial_z^2). \quad (44)$$

Thus, we need the two dot products in (43) to be in proportion with a ratio of 2 : 1, which simplifies to the following constraint:

$$\mathbf{v}_1 \cdot \boldsymbol{\alpha} = 0, \quad \mathbf{v}_1 := (2, -1, 8, -4, 2, 18)^T. \quad (45)$$

In other words, the above is a constraint for fourth-order isotropy in $\delta_{\Delta,62}$, for some C_1 to be specified shortly.

Carrying on with this procedure for sixth-order isotropy—i.e., expanding $\delta_{\Delta,62}$ to sixth-order in X and associating terms to the triharmonic (leaving out steps for brevity)—we obtain the following two additional constraints:

$$\mathbf{v}_2 \cdot \boldsymbol{\alpha} = 0, \quad \mathbf{v}_2 := (-2, 3, -32, 8, -6, -162)^T, \quad (46a)$$

$$\mathbf{v}_3 \cdot \boldsymbol{\alpha} = 0, \quad \mathbf{v}_3 := (0, 1, 0, -4, 4, 0)^T. \quad (46b)$$

Under these isotropy constraints, the scheme expands to:

$$\delta_{tt} - c^2 \delta_{\Delta,62} = \partial_t^2 - c^2 \Delta + r_1 T^2 \partial_t^4 - c^2 X^2 C_1 \Delta^2 + r_2 T^4 \partial_t^6 - c^2 X^4 C_2 \Delta^3 + \mathcal{O}(T^6) + \mathcal{O}(X^6), \quad (47)$$

where $r_1 = 1/12$ and $r_2 = 1/360$, and where C_1 and C_2 are now given as:

$$C_1 = r_1 \mathbf{c}_1 \cdot \boldsymbol{\alpha}, \quad \mathbf{c}_1 := (1, 1, 4, 1, 17/5, 9)^T, \quad (48a)$$

$$C_2 = r_2 \mathbf{c}_2 \cdot \boldsymbol{\alpha}, \quad \mathbf{c}_2 := (1, 1, 16, 1, 13, 81)^T. \quad (48b)$$

2) *High-order accuracy*: From here, our goal is to arrive at fourth-order or sixth-order accuracy, which effectively means that the finite difference operators will expand to:

$$\delta_{tt} - c^2 \delta_{\Delta,62} = \partial_t^2 - c^2 \Delta + \mathcal{O}(X^{2M}) + \mathcal{O}(T^{2M}). \quad (49)$$

with $M = 2$ or $M = 3$. Since the above equation is also equal to zero (by the definition of our scheme; i.e., (9) with $\delta_{\Delta} = \delta_{\Delta,62}$), our scheme solves a modified equation of the form (23) for $M \leq 3$. It is easy to show that (23) implies the following for any M :

$$\partial_t^4 - c^4 \Delta^2 = \mathcal{O}(X^{2M}), \quad (50a)$$

$$\partial_t^6 - c^6 \Delta^3 = \mathcal{O}(X^{2M}). \quad (50b)$$

Using the above relations we can substitute for ∂_t^4 and ∂_t^6 in (47) to obtain the following expansion:

$$\delta_{tt} - c^2 \delta_{\Delta,62} = \partial_t^2 - c^2 \Delta + r_1 X^2 (\lambda^2 - \mathbf{c}_1 \cdot \boldsymbol{\alpha}) c^2 \Delta^2 + r_2 X^4 (\lambda^4 - \mathbf{c}_2 \cdot \boldsymbol{\alpha}) c^4 \Delta^3 + \mathcal{O}(T^6) + \mathcal{O}(X^6). \quad (51)$$

At this point it is clear that we can eliminate $\mathcal{O}(X^2)$ and $\mathcal{O}(X^4)$ terms through the following additional constraints:

$$\mathbf{c}_1 \cdot \boldsymbol{\alpha} = \lambda^2, \quad \mathbf{c}_2 \cdot \boldsymbol{\alpha} = \lambda^4, \quad (52)$$

which gives our desired result. In other words, we have arrived at (49) with $M = 2$ or $M = 3$, leaving truncation errors that are $\mathcal{O}(X^4)$ or $\mathcal{O}(X^6)$ for this family of schemes.

To summarize, our finite difference scheme expands to (49) where $M \geq 1$ (in general), but under the constraints described by the following overdetermined system:

$$(\mathbf{1}|\mathbf{v}_1|\mathbf{c}_1)^T \boldsymbol{\alpha} = (1, 0, \lambda^2)^T \quad (53)$$

we have $M = 2$ (a fourth-order truncation error); and furthermore, under the constraints described by:

$$(\mathbf{1}|\mathbf{v}_1|\mathbf{v}_2|\mathbf{v}_3|\mathbf{c}_1|\mathbf{c}_2)^T \boldsymbol{\alpha} = (1, 0, 0, 0, \lambda^2, \lambda^4)^T \quad (54)$$

we have $M = 3$ (a sixth-order truncation error).

B. Example high-order accurate schemes and coefficients

What follows are three schemes that are able to achieve fourth-order accuracy, along with a sixth-order accurate scheme. These schemes represent particular solutions to the linear systems above. Of course, in order to fully achieve high-order accuracy a scheme must also be stable, so numerical stability conditions will be provided alongside the particular schemes to follow. However, for brevity we will omit detailed stability derivations, as they can be lengthy, particularly due to the fact that the simplified conditions (15) will not apply for the high-order accurate schemes to follow, as the associated functions F are polynomials in \hat{s}_w and λ^2 , and evaluating (14) can become quite involved.

It should also be mentioned that the first and last schemes considered next have previously been derived by related modified equation approaches [50], but they have yet to be considered for room acoustics simulation. Subsequent to presenting the coefficients for these schemes, we will analyze numerical dispersion and compare to the compact explicit schemes and large-star schemes.

1) *A 25-point fourth-order accurate scheme*: The smallest two-step explicit scheme that can achieve fourth-order accuracy employs the stencil illustrated in Fig. 7(a) [47], [50]. Solving (53) under the additional constraints: $\alpha_4 = \alpha_5 = \alpha_6 = 0$, the coefficients for this scheme are found to be:

$$\alpha_1 = 1 - \alpha_2 - \alpha_3, \quad \alpha_2 = 8r_1 \lambda^2, \quad \alpha_3 = 4r_1 (\lambda^2 - 1), \quad (55)$$

or in terms of the coefficients a_1, a_2, a_3 [50]:

$$a_1 = 1, \quad a_2 = 2r_1 \lambda^2, \quad a_3 = r_1 (\lambda^2 - 1). \quad (56)$$

It is worth noting that under the above constraints, the discrete Laplacian can be rewritten as [47]:

$$\delta_{\Delta} = \delta_{\Delta}^{(2)} + r_1 c^2 T^2 \delta_{\Delta}^{(1)} \delta_{\Delta}^{(1)}. \quad (57)$$

In a sense, the above shows that this scheme augments the fourth-order-in-space large-star scheme from Section III with an appropriately scaled second-order accurate approximation to the biharmonic operator ($\delta_{\Delta}^{(1)} \delta_{\Delta}^{(1)} = \Delta^2 + \mathcal{O}(X^2)$), which, in effect, leads to a cancellation with the second-order error term that arises in δ_{tt} [47], [50]. With regards to numerical stability, from (57) it is straightforward to derive the condition for this scheme: $\lambda \leq \sqrt{1/3}$ [50]. That this scheme is indeed fourth-order accurate is confirmed in Fig. 8.

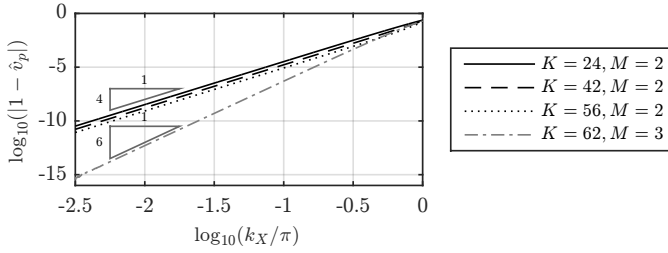


Fig. 8: Relative dispersion error as a function of wavenumber along axial directions for $2M$ th-order accurate $(K+1)$ -point schemes presented in this section, with Courant numbers set to respective upper stability limits.

2) *A 43-point fourth-order accurate scheme:* Consider the 43-point stencil illustrated in Fig. 7(b), as given by the constraints $\alpha_3 = \alpha_4 = \alpha_6 = 0$. Solving (53) under these additional constraints leads to:

$$\alpha_1 = 1 - \alpha_2 - \alpha_5, \quad \alpha_2 = 2/3, \quad \alpha_5 = 5r_1(\lambda^2 - 1), \quad (58)$$

or a_1, a_2, a_3 given by (56) and

$$a_4 = 0, \quad a_5 = (\lambda^2 - 1)/48, \quad a_6 = 0. \quad (59)$$

Through an exhaustive analysis of the associated function F (left out for brevity), the stability condition is found to be: $\lambda^2 \leq (3 - \sqrt{3})/2 \approx 0.796$. Also, see Fig. 8.

3) *A 57-point fourth-order accurate, sixth-order isotropic scheme:* Consider the 57-point stencil illustrated in Fig. 7(c). Given the number of free parameters, we can aim for a fourth-order accuracy and sixth-order isotropy. As such, we solve the following system, along with the constraint $\alpha_6 = 0$:

$$(1|\mathbf{v}_1|\mathbf{v}_2|\mathbf{v}_3|\mathbf{c}_1)^T \boldsymbol{\alpha} = (1, 0, 0, 0, \lambda^2)^T. \quad (60)$$

This gives the following coefficients:

$$\alpha_2 = 8r_2(72 - 40\lambda^2), \quad \alpha_3 = 8r_2(9 - 5\lambda^2), \\ \alpha_4 = 24r_2(5\lambda^2 - 4), \quad \alpha_5 = 40r_2(5\lambda^2 - 6), \quad (61)$$

and $\alpha_1 = 1 - \alpha_2 - \alpha_3 - \alpha_4 - \alpha_5$. Equivalently, a_1, a_2, a_3 are given by (56) and

$$a_4 = 6r_2(5\lambda^2 - 4), \quad a_5 = 2r_2(5\lambda^2 - 6), \quad a_6 = 0. \quad (62)$$

Through analysis of the associated F , the stability condition for this scheme is found to be: $4/15 \leq \lambda^2 \leq 3(6 - \sqrt{11})/10 \approx 0.896$, where the lower bound on the Courant number results from evaluating the condition $F \geq 0$. See Fig. 8.

4) *A 63-point sixth-order accurate scheme:* For sixth-order accuracy, we will need the entire set of free parameters in this family of schemes, and thus the stencil illustrated in Fig. 7(d). Solving (54) gives:

$$\alpha_2 = 8r_1\lambda^2 + r_2(160\lambda^2 - 144\lambda^4), \quad \alpha_4 = 24r_2\lambda^4, \\ \alpha_5 = r_2(60\lambda^4 - 100\lambda^2), \quad \alpha_6 = r_2(9\lambda^4 - 45\lambda^2 + 36), \\ \alpha_3 = r_1(4\lambda^2 - 4) + r_2(200\lambda^2 - 72\lambda^4 - 96), \quad (63)$$

and $\alpha_1 = 1 - \alpha_2 - \alpha_3 - \alpha_4 - \alpha_5 - \alpha_6$. Equivalently, a_1, a_2, a_3 are given by (56) and:

$$a_4 = 6r_2\lambda^4, \quad a_5 = r_2(3\lambda^4 - 5\lambda^2), \quad a_6 = r_2(\lambda^4 - 5\lambda^2 + 4). \quad (64)$$

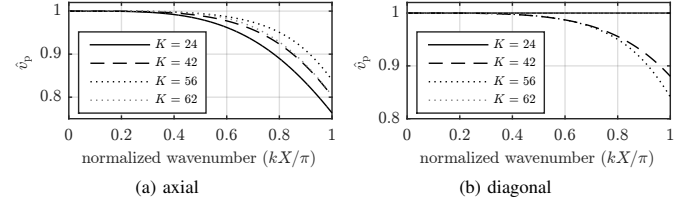


Fig. 9: Relative phase velocities for $(K+1)$ -point high-order accurate schemes with $\lambda = \lambda_{\max}$ and for wavenumbers $k_X \leq \pi$ along (a) axial and (b) diagonal directions.

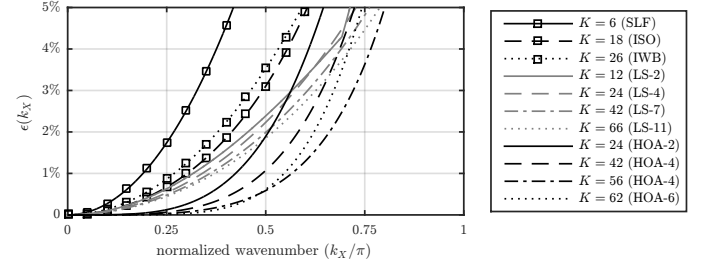


Fig. 10: Comparisons of various $(K+1)$ -point schemes in terms of cumulative max error $\epsilon(k_X)$. Large-star schemes are denoted “LS- M ”, where $K = 6M$, and “HOA- Q ” refers to the high-order accurate schemes from Section IV with Q th-order accuracy.

For this scheme, it can be shown that numerical stability is ensured when $\lambda \leq \sqrt{1/3}$ [50]. See Fig. 8 for confirmation that this scheme is indeed sixth-order accurate.

V. COMPARISONS: NUMERICAL DISPERSION

So far we have derived four high-order accurate schemes and confirmed their reported orders of accuracy (in Fig. 8). However, this only gives an indication as to how the schemes behave as k_X approaches zero, whereas for room acoustics we are also interested in the numerical dispersion over a wide range of frequencies, extending from DC towards the Nyquist. With that said, numerical phase velocities for the high-order accurate schemes presented in this section are displayed in Fig. 9 over the range of wavenumbers $k_X \in [0, \pi]$. Immediately, it can be seen that in the range of $k_X \leq 0.25\pi$ there are substantial improvements over the SLF, ISO, IWB, and large-star schemes (in Figs. 2 and 5). For $k_X \in [0.25\pi, \pi]$ it is difficult to visually discern from these figures how these schemes compare to the second-order accurate schemes from Sections II and III, so we need to quantify these dispersion error in some other meaningful way.

To that end, we introduce a cumulative maximum error for the relative phase velocity:

$$\epsilon(k_X) := \max_{|\mathbf{k}'_X| \in [0, k_X]} |1 - \hat{v}_p(\mathbf{k}'_X)|, \quad (65)$$

where $0 < k_X \leq \pi$. In Fig. 10, we plot $\epsilon(k_X)$ for various schemes (leaving out some large-star schemes, for clarity); and we focus on $\epsilon(k_X) \leq 5\%$ —for brevity, and because there is recent evidence that high-fidelity auralizations require phase velocities errors to be as low as 2% to mitigate audible phase artifacts [18]. From Fig. 10 we can conclude the following: under equivalent memory costs,

TABLE I: Relative computational efficiency (RCE), defined by (66), allowing at most $P\%$ absolute error in phase velocity in $(K + 1)$ -point schemes. The notation: $[\lambda]_3$ denotes λ truncated to three decimal places.

scheme	K	$[\lambda]_3$	0.1%	0.5%	1%	2%	4%	8%
SLF	6	0.577	1.00	1.00	1.00	1.00	1.00	1.00
ISO	18	0.866	10.5	10.06	9.51	8.57	7.12	5.30
IWB	26	1.000	6.93	6.93	6.93	6.93	6.94	6.97
LS-2	12	0.500	6.21	6.40	6.66	7.21	8.50	4.37
LS-3	18	0.469	7.40	7.31	7.22	7.10	7.04	6.51
LS-4	24	0.452	8.26	8.14	8.00	7.74	7.34	6.92
LS-7	42	0.428	9.76	9.62	9.45	9.11	8.48	7.42
LS-11	66	0.414	10.8	10.6	10.5	10.1	9.37	8.10
HOA-4	24	0.577	233	48.0	24.7	12.9	6.88	3.84
HOA-4	42	0.796	620	123	61.6	30.8	15.4	7.82
HOA-4	56	0.897	1331	253	122	57.7	26.8	12.3
HOA-6	62	0.577	1296	163	68.2	29.1	12.8	5.96

- the large-star schemes ($1 < M \leq 11$) outperform compact explicit schemes—at least for $\epsilon(k_X) \leq 5\%$;
- the high-order accurate schemes generally outperform large-star schemes for $k_X \leq 0.5\pi$;
- the high-order accurate schemes generally outperform large-star schemes for $\epsilon(k_X) \leq 2\%$;
- for $\epsilon(k_X) \in [2\%, 5\%]$, the high-order accurate schemes tend to outperform large-star schemes of equivalent or larger stencil size;

and, as expected, the high-order accurate schemes increasingly outperform second-order accurate schemes as $\epsilon(k_X) \rightarrow 0$ or as $k_X \rightarrow 0$.

It is important to remember that the high-order accurate schemes have the advantage of operating with significantly higher Courant numbers than the large-star schemes, and thus lower sample rates for the same grid density. To take this into account directly in the comparisons, we can make use of the *relative computational efficiency* (RCE) metric described in [3], [53], which compares schemes in terms of *spatiotemporal* grid densities required to maintain a given error threshold over some bandwidth of interest. We can define this RCE as:

$$\text{RCE}(P\%) := \frac{\lambda}{\lambda_{\max, \text{SLF}}} \left(\frac{\max_{k_X} \text{ s.t. } \epsilon(k_X) \leq P\%}{\max_{k_X} \text{ s.t. } \epsilon(k_X) \leq P\% \text{ in SLF}} \right)^4, \quad (66)$$

where the SLF scheme serves as a common reference of comparison, as in [3]. RCEs for some error thresholds between 0.1% and 8% are listed in Table I for the schemes displayed in Fig. 10. We find that the HOA schemes outperform compact explicit and large-star schemes by up to three orders of magnitude in their RCEs for the %-errors listed. Interestingly, we also find that the compact explicit schemes sometimes outperform large-star schemes in terms of RCEs. For example, if a maximum 2% phase velocity error is deemed necessary, Table I indicates that the 19-point ISO scheme is a better choice than 19-point and 25-point large-star schemes—that is, if the interest is in minimizing the number of pointwise updates required by the scheme, and not just memory costs.

VI. COMPARISONS: SIMULATIONS

A. Modes of a rigid cuboid room

In order to demonstrate how the dispersion errors in the various schemes manifest in simulation outputs, consider,

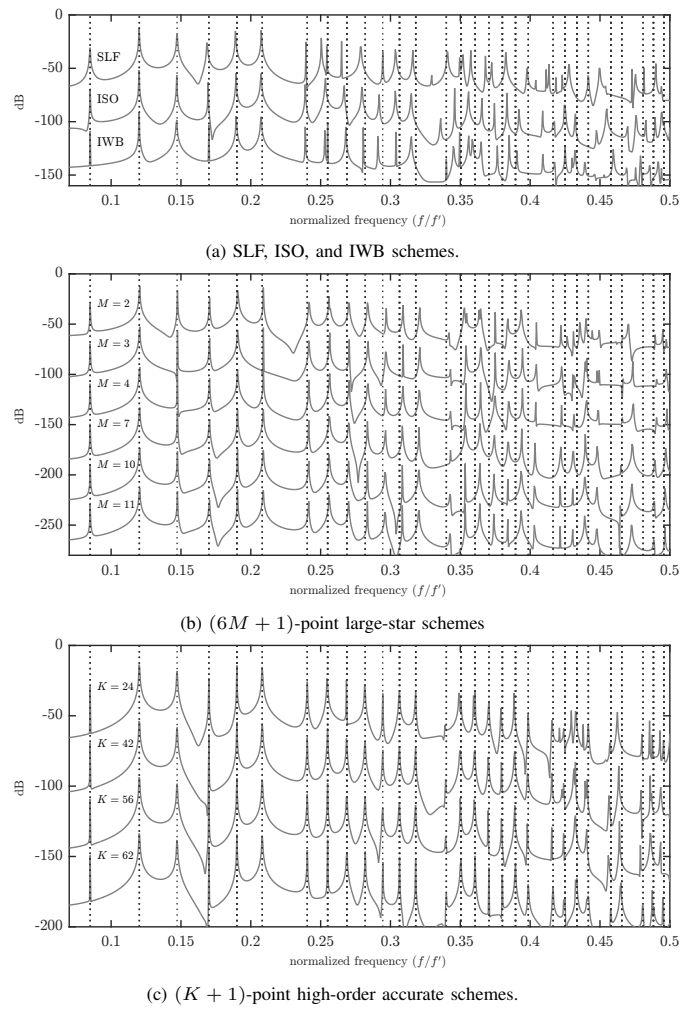


Fig. 11: Simulated responses of cuboid room with side-length 10 m and rigid boundaries, along with analytic modes (dotted lines). Responses are shifted by 50 dB for clarity, and the frequencies are normalized by $f' = \frac{c}{2X} = 200$ Hz.

as a simple first example, the modal response of a cuboid room under rigid boundary conditions. For this example, we consider a cubic room with side-length 10 m, and for all schemes we keep $X = 0.85$ m and sample rates are set according to respective stability limits (i.e., $F_s = \frac{c}{2X}$, and see Table I). In this idealized scenario, boundary conditions can be implemented by forcing ghost points to be even-symmetric with interior points.⁴ The box is excited with an off-center spatial Gaussian and outputs of duration 10 s are taken near a corner of the room.

The simulated responses—transformed to frequency domain via discrete Fourier transform without zero-padding—can be seen in Fig. 11, wherein they are shown as a function of normalized frequencies $f/f' \leq 0.5$ with $f' = \frac{c}{2X} = 200$ Hz representing the frequency associated to the isotropic spatial bandlimit of the Cartesian grid used here [40]. It can be seen that all schemes correctly approximate modal frequencies in low frequencies (indicating that the schemes are consistent for

⁴Numerical stability is ensured in this special case because the simulated modes are spatial cosines that can be decomposed into plane-wave solutions, which are covered by von Neumann stability analyses.

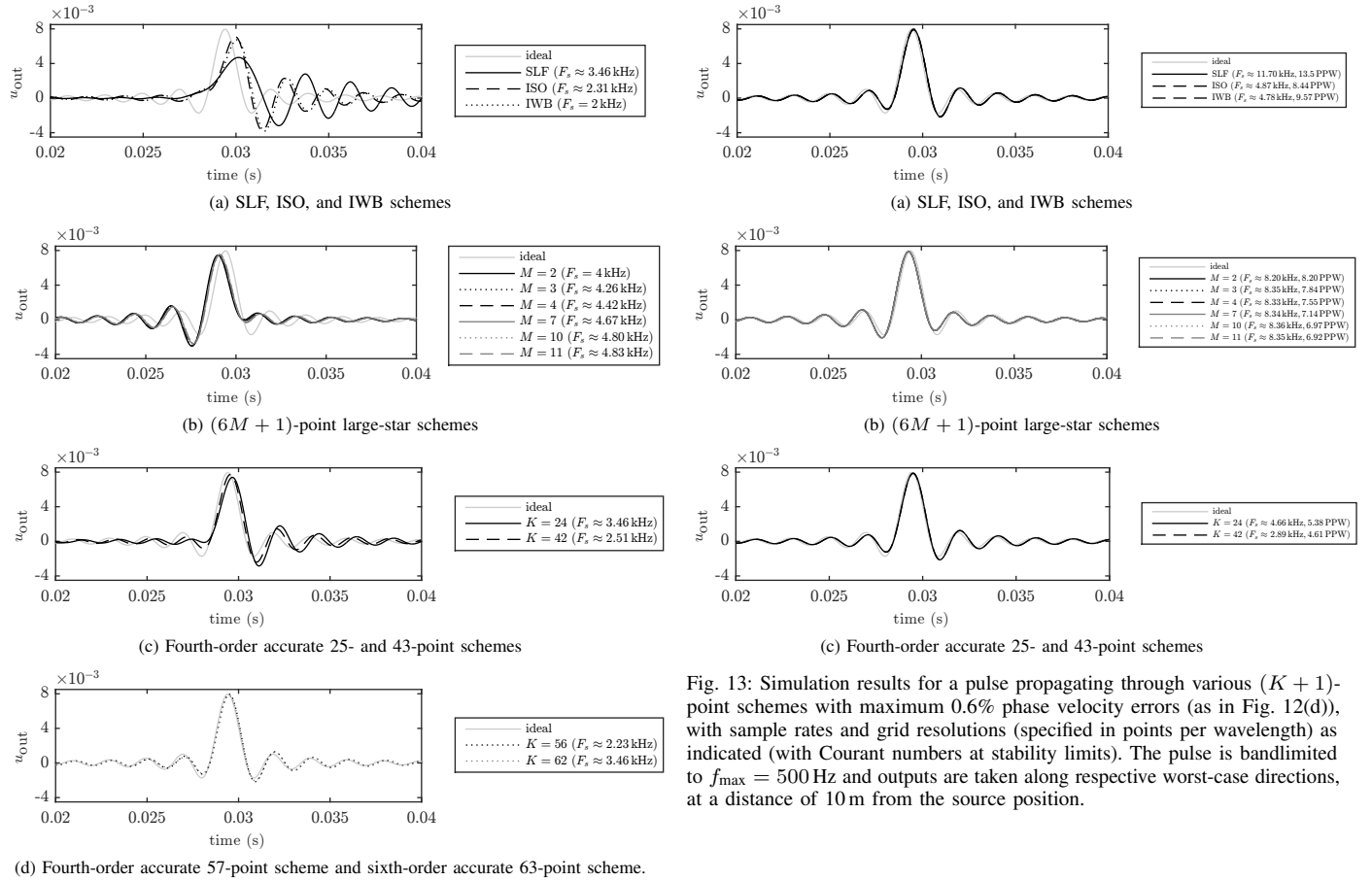


Fig. 12: Demonstration of numerical dispersion in a pulse propagating through various $(K+1)$ -point schemes under equivalent memory costs. The pulse is bandlimited to $f_{\max} = 500$ Hz and outputs are taken along respective worst-case directions, at 10 m from source position. Grid spacings are $X = \frac{c}{4f_{\max}}$ (four points per wavelength), and sample rates are as indicated (Courant numbers at stability limits).

this problem and boundary implementation) and mismatches tend to increase with f/f' . For $f/f' > 0.25$, the second-order accurate schemes (including large-star schemes) are unable to simulate correct modal frequencies, but the high-order accurate schemes return good matches until at least $f/f' \approx 0.4$. It can also be seen that modal responses in large-star schemes do not improve significantly with increasing spatial order $2M$, which is ultimately due to a temporal error that remains second-order throughout.

B. Free-space propagation

In order to demonstrate how dispersion errors affect free-space propagation of waves in these schemes, we consider an unbounded problem with initial conditions $u(0, \mathbf{x}) = 0$ and $\partial_t u(t, \mathbf{x})|_{t=0} = V_0 c^2 \delta(\mathbf{x})$ where V_0 is a source volume—without loss of generality, taken to be 1 m^3 —and $\delta(\mathbf{x})$ represents a 3-D spatial Dirac delta. In this case, u represents an acoustic velocity potential (in $\text{m}^2 \text{s}^{-1}$) [54]. For discrete initial conditions, we take $u_l^0 = 0$, and in order to mitigate possible errors from initialization, we compute u_l^1 from the known solution [55] (bandlimited to the Cartesian grid). For this example, we consider only $k_X \leq 0.5\pi$ (i.e., we use at

Fig. 13: Simulation results for a pulse propagating through various $(K+1)$ -point schemes with maximum 0.6% phase velocity errors (as in Fig. 12(d)), with sample rates and grid resolutions (specified in points per wavelength) as indicated (with Courant numbers at stability limits). The pulse is bandlimited to $f_{\max} = 500$ Hz and outputs are taken along respective worst-case directions, at a distance of 10 m from the source position.

least four points per wavelength) and we focus on a maximum frequency of $f_{\max} = 500$ Hz. Thus, the grid spacing is chosen as $X = c/4f_{\max}$ for all schemes, and $T = X\lambda/c$ where λ is chosen respectively at upper stability limits for each scheme. Shown in Fig. 12 are numerical solutions obtained from the various schemes, at output positions along respective worst-case directions (axial for SLF and ISO, and diagonal for IWB; diagonal for large-star schemes; axial for high-order accurate schemes with $K = 24, 42, 62$ and diagonal for $K = 56$) at a distance of 10 m from the source position, along with the corresponding (bandlimited) analytical solution. It is important to remember that here memory costs are equivalent across schemes, but sample rates vary according to respective λ .

The effect of phase velocity errors in these schemes is most apparent in Fig. 12(a), with visible deviations between the ideal solution and numerical solutions. The ISO and IWB schemes appear to give similar results along their respective worst-case directions, and the SLF scheme returns significantly worse results. Across the large-star schemes in Fig. 12(b), results are similar, and Fig. 12(b) represents an improvement over SLF, ISO, and IWB schemes—at the cost of higher sample rates. We also note the numerical approximations in Fig. 12(b) are advanced-in-time with respect to the ideal solution, which is a result of the phase velocities along the chosen propagation direction (diagonal). Finally, the high-order accurate schemes, in Fig. 12(c) and Fig. 12(d) tend to give the best results—particularly for $K \in \{56, 62\}$ in Fig. 12(d)—while operating at significantly lower sample rates than large-star schemes.

While we have found that the high-order accurate schemes

performed best under equivalent memory costs for this example, it is also worth checking how all schemes compare under equivalent error tolerances, which requires that grid densities and sample rates vary across schemes. As a point of reference, we can use the results in Fig. 12(d), for which the schemes are set up with approximately $\epsilon(k_X) = 0.6\%$ for $\frac{ck_X}{2\pi} = 500$ Hz. As such, we re-calibrate the other schemes to have the same maximum phase velocity error at the same corresponding wavenumber. Results are displayed in Fig. 13, with sample rates and grid resolutions—specified in points per wavelength (PPW)—as indicated. Recall, memory costs scale cubically with the grid resolution in PPW.

As one might expect, all schemes now return similar results to those in Fig. 12(d), but we see that the high-order accurate schemes use significantly lower grid resolutions and sample rates than compact explicit and large-star schemes to obtain such results. For example, the 25-point fourth-order accurate scheme uses approximately $5.6\times$ less memory than the 27-point IWB scheme, and $2.8\times$ less memory than the large-star scheme with same stencil size ($M = 4$). We also note that the fourth-order accurate scheme with $K = 42$ uses approximately $3.7\times$ less memory than the large-star scheme with same stencil size ($M = 7$). To quantify how “similar” these results are—beyond what can be discerned visually—we can report that residual errors are all between -22 dB and -20 dB in signal-to-noise-ratio (SNR), but we should also remark that SNR is not necessarily a good indicator of performance here, since the residual is highly correlated with the signal itself, although a detailed perceptual examination of such residuals is beyond the scope of this study (see, e.g., [18]).

VII. CONCLUSIONS AND FINAL REMARKS

We have presented high-order accurate schemes for the 3-D wave equation derived through the use of modified equation methods, reaching up to sixth-order accuracy with a 63-point stencil, along with fourth-order accurate schemes with 25-, 43-, and 57-point stencils. As opposed to large-star schemes that employ high-order spatial differences yet are limited by a second-order temporal accuracy, these schemes possess high orders of accuracy in both space and time, and as a result, display high-order rates of convergence in their numerical dispersion relations, confirming that they are indeed high-order accurate for the 3-D wave equation. Numerical phase velocities were analyzed for these schemes along with previously considered second-order accurate schemes (which includes large-star schemes), and it was shown that the high-order accurate schemes are significantly more computationally efficient when low error tolerances in numerical phase velocities (e.g., less than 2%) are critical—as is the case for high-fidelity auralizations. In order to confirm the performance of these schemes, example simulations were conducted, including modal responses of a rigid box and free-space pulse propagation. As compared to second-order counterparts, with memory costs fixed the high-order schemes returned more accurate approximations (closer to analytical solutions); and similarly, with a prescribed accuracy in the approximations, the high-order schemes were able to operate with significantly less computational costs than second-order counterparts.

There are many avenues for further investigation. First, large-star schemes are known to benefit from operating with Courant numbers below stability limits, at the cost of even higher sample rates [45]—in contrast to the compact explicit schemes and the high-order accurate schemes presented here. This could not be considered in this study, as it is an optimization that must be tuned to error metrics of interest; see [56], [57]. The family of schemes we have presented (based on the discrete Laplacian (37)) can also benefit from optimization (e.g., following [41]), where degrees of high order accuracy and isotropy can be traded for the pursuit of higher RCEs at fixed error tolerances (as in [52]; see also [57]). Decimation-in-time techniques could also be investigated as a further means of saving computation [58].

Parallel implementations on GPUs could also be investigated in future work. To that end, it is worth remarking that there are no significant additional bottlenecks for schemes that use large stencils [34], such as those presented here, as compared to those with smaller stencils, such as the 7-point SLF scheme or 27-point compact explicit schemes. This is because in GPU implementations of large-scale room acoustics simulations, the main bottleneck tends to be memory accesses and limited memory bandwidth, and while larger stencils require more memory accesses from neighboring grid points, this is mitigated by memory cache effects (as demonstrated in [34]). Ultimately, this is due to the fact that as stencil sizes increase, so does the number of neighboring points that are shared between neighboring point-wise updates.

Perhaps the most important area of future work is the formulation of consistent and stable grid truncation with impedance boundaries over complex geometries for these schemes, and indeed, this constitutes a major challenge for any scheme that employs stencils reaching beyond nearest grid neighbors. Boundary updates for half-spaces aligned with Cartesian axes could possibly be derived following the frequency-domain techniques used in [3], but such techniques do not necessarily extend to non-cuboid rooms (see, e.g., [59] and [57, Chapter 5]). One could resort to perfectly matched layer (PML)–based boundaries (as in, e.g., [60]), although open problems with such techniques include consistency with realistic room models and numerical stability. Another possible approach might be to investigate finite volume generalizations of the presented FDTD schemes, as this has already proven to be useful for some nearest-neighbor FDTD schemes [27], [61]. With any of these approaches, maintaining high-order accuracy at boundaries may be an additional concern. Including viscothermal losses in air (classical air absorption) is a straightforward extension (see [25]) but it should be noted that explicit two-step schemes are reduced to first-order accuracy. However, maintaining high-order accuracy for losses at walls and in air may not be so important (as long as consistency can be achieved), since general improvements to dispersion would be unchanged in the wideband sense.

REFERENCES

- [1] D. Botteldooren, “Finite-difference time-domain simulation of low-frequency room acoustic problems,” *J. Acoustical Society of America*, vol. 98, pp. 3302–3308, 1995.

- [2] L. Savioja, T. J. Rinne, and T. Takala, "Simulation of room acoustics with a 3-D finite difference mesh," in *Proc. ICMC*, Danish Institute of Electroacoustic Music, Denmark, 1994, pp. 463–466.
- [3] K. Kowalczyk and M. van Walstijn, "Room acoustics simulation using 3-D compact explicit FDTD schemes," *IEEE TASLP*, vol. 19, no. 1, pp. 34–46, 2011.
- [4] V. Välimäki, J. D. Parker, L. Savioja, J. O. Smith III, and J. S. Abel, "Fifty years of artificial reverberation," *IEEE TASLP*, vol. 20, no. 5, pp. 1421–1448, 2012.
- [5] S. Kitić, N. Bertin, and R. Gribonval, "Hearing behind walls: localizing sources in the room next door with cosparsity," in *Proc. IEEE ICASSP*, 2014, pp. 3087–3091.
- [6] N. Antonello, T. van Waterschoot, M. Moonen, and P. A. Naylor, "Source localization and signal reconstruction in a reverberant field using the fddt method," in *Proc. EUSIPCO*, 2014, pp. 301–305.
- [7] N. Bertin, S. Kiti, and R. Gribonval, "Joint estimation of sound source location and boundary impedance with physics-driven cosparsity regularization," in *Proc. IEEE ICASSP*, 2016, pp. 6340–6344.
- [8] N. Antonello, T. van Waterschoot, M. Moonen, and P. A. Naylor, "Identification of surface acoustic impedances in a reverberant room using the FDTD method," in *IEEE International Workshop on Acoustic Signal Enhancement (IWAENC)*, 2014, pp. 114–118.
- [9] R. Mehra and D. Manocha, "Wave-based sound propagation for VR applications," in *IEEE Virtual Reality*, Minnesota, USA, 2014.
- [10] L. Savioja and U. P. Svensson, "Overview of geometrical room acoustic modeling techniques," *J. Acoustical Society of America*, vol. 138, no. 2, pp. 708–730, 2015.
- [11] N. Röber, M. Spindler, and M. Masuch, "Waveguide-based room acoustics through graphics hardware," in *Proc. ICMC*, 2006.
- [12] C. J. Webb and S. Bilbao, "Computing room acoustics with CUDA - 3D FDTD schemes with boundary losses and viscosity," in *Proc. IEEE ICASSP*, Prague, Czech Republic, 2011, pp. 317–320.
- [13] C. Spa, A. Rey, and E. Hernandez, "A GPU implementation of an explicit compact FDTD algorithm with a digital impedance filter for room acoustics applications," *IEEE/ACM TASLP*, vol. 23, no. 8, pp. 1368–1380, 2015.
- [14] J. A. Hargreaves, *Time Domain Boundary Element Method for Room Acoustics*, Ph.D. thesis, University of Salford, 2007.
- [15] T. Sakuma, S. Sakamoto, and T. Otsuru, *Computational Simulation in Architectural and Environmental Acoustics*, Springer, 2014.
- [16] A. Southern, S. Siltanen, D. T. Murphy, and L. Savioja, "Room impulse response synthesis and validation using a hybrid acoustic model," *IEEE TASLP*, vol. 21, no. 9, pp. 1940–1952, 2013.
- [17] H. Yeh, R. Mehra, Z. Ren, L. Antani, D. Manocha, and M. Lin, "Wave-ray coupling for interactive sound propagation in large complex scenes," *ACM Transactions on Graphics (TOG)*, vol. 32, no. 6, pp. 165, 2013.
- [18] J. Saarelma, J. Botts, B. Hamilton, and L. Savioja, "Audibility of dispersion error in room acoustic finite-difference time-domain simulation as a function of simulation distance," *J. Acoustical Society of America*, vol. 139, no. 4, pp. 1822–1832, 2016.
- [19] G. R. Campos and D. M. Howard, "On the computational efficiency of different waveguide mesh topologies for room acoustic simulation," *IEEE TSAP*, vol. 13, no. 5, pp. 1063–1072, 2005.
- [20] D. T. Murphy, A. Kelloniemi, J. Mullen, and S. Shelley, "Acoustic modeling using the digital waveguide mesh," *IEEE Signal Processing Magazine*, vol. 24, no. 2, pp. 55–66, 2007.
- [21] J. van Mourik and D. Murphy, "Explicit higher-order FDTD schemes for 3D room acoustic simulation," *IEEE/ACM TASLP*, vol. 22, no. 12, pp. 2003–2011, 2014.
- [22] K. Kowalczyk and M. van Walstijn, "A comparison of nonstaggered compact FDTD schemes for the 3D wave equation," in *Proc. IEEE ICASSP*, Dallas, Texas, 2010, pp. 197–200.
- [23] B. Hamilton, S. Bilbao, and C. J. Webb, "Revisiting implicit finite difference schemes for 3-D room acoustics simulations on GPU," in *Proc. Digital Audio Effects (DAFx)*, Erlangen, Germany, Sept. 2014, pp. 41–48.
- [24] L. E. Kinsler, A. R. Frey, A. B. Coppens, and J. V. Sanders, *Fundamentals of Acoustics*, John Wiley & Sons, 4th edition, 2000.
- [25] B. Hamilton, S. Bilbao, and C. J. Webb, "Improved finite difference schemes for a 3-D viscothermal wave equation on a GPU," in *Proc. Forum Acusticum*, Krakow, Poland, 2014.
- [26] S. Bilbao and B. Hamilton, "Wave-based room acoustics simulation: Explicit/implicit finite volume modeling of viscothermal losses and frequency-dependent boundaries," *J. Audio Engineering Society*, vol. 65, no. 1/2, pp. 78–89, 2017.
- [27] S. Bilbao, B. Hamilton, J. Botts, and L. Savioja, "Finite volume time domain room acoustics simulation under general impedance boundary conditions," *IEEE/ACM TASLP*, vol. 24, no. 1, pp. 161–173, 2016.
- [28] J. Botts and L. Savioja, "Effects of sources on time-domain finite difference models," *J. Acoustical Society of America*, vol. 136, no. 1, pp. 242–247, 2014.
- [29] A. Southern, D. T. Murphy, and L. Savioja, "Spatial encoding of finite difference time domain acoustic models for auralization," *IEEE TASLP*, vol. 20, no. 9, pp. 2420–2432, 2012.
- [30] J. Sheaffer, M. Van Walstijn, B. Rafaely, and K. Kowalczyk, "Binaural reproduction of finite difference simulations using spherical array processing," *IEEE/ACM TASLP*, vol. 23, no. 12, pp. 2125–2135, 2015.
- [31] S. Bilbao and B. Hamilton, "Directional source modeling in wave-based room acoustics simulation," in *Proc. IEEE WASPAA*, New Paltz, NY, USA, Oct. 2017.
- [32] S. Bilbao and J. O. Smith III, "Finite difference schemes and digital waveguide networks for the wave equation: Stability, passivity, and numerical dispersion," *IEEE TSAP*, vol. 11, no. 3, pp. 255–266, 2003.
- [33] L. Savioja and V. Välimäki, "Interpolated rectangular 3-D digital waveguide mesh algorithms with frequency warping," *IEEE TSAP*, vol. 11, no. 6, pp. 783–790, 2003.
- [34] B. Hamilton, C. J. Webb, A. Gray, and S. Bilbao, "Large stencil operations for GPU-based 3-D acoustics simulations," in *Proc. Digital Audio Effects (DAFx)*, Trondheim, Norway, Dec. 2015, pp. 292–299.
- [35] G. E. Forsythe and W. R. Wasow, *Finite-difference Methods for Partial Differential Equations*, pp. 378–382, New York: Wiley, 1960.
- [36] S. A. van Duyn and J. O. Smith III, "Physical modeling with the 2-D digital waveguide mesh," in *Proc. ICMC*, Tokyo, Japan, 1993.
- [37] S. Bilbao, *Wave and Scattering Methods for the Numerical Integration of Partial Differential Equations*, Ph.D. thesis, Stanford University, 2001.
- [38] J. Strikwerda, *Finite Difference Schemes and Partial Differential Equations*, SIAM, Philadelphia, PA, 2004.
- [39] G. G. O'Brien, M. A. Hyman, and S. Kaplan, "A study of the numerical solution of partial differential equations," *J. Mathematical Physics*, vol. 29, pp. 223–251, 1950.
- [40] D. P. Petersen and D. Middleton, "Sampling and reconstruction of wave-number-limited functions in N-dimensional Euclidean spaces," *Information and Control*, vol. 5, no. 4, pp. 279–323, 1962.
- [41] S. Bilbao, "Optimized FDTD schemes for 3-D acoustic wave propagation," *IEEE TASLP*, vol. 20, no. 5, pp. 1658–1663, 2012.
- [42] J. O. Smith III, "Physical modeling using digital waveguides," *Computer Music Journal*, vol. 16, no. 4, pp. 74–91, 1992.
- [43] W. F. Ames, *Numerical Methods for Partial Differential Equations*, Academic Press, 2nd edition, 1977.
- [44] S. Bilbao, *Numerical Sound Synthesis: Finite Difference Schemes and Simulation in Musical Acoustics*, Wiley, 2009.
- [45] M. A. Dablain, "The application of high-order differencing to the scalar wave equation," *Geophysics*, vol. 51, no. 1, pp. 54–66, 1986.
- [46] L. Anné, Q. H. Tran, and W. W. Symes, "Dispersion and cost analysis of some finite difference schemes in one-parameter acoustic wave modeling," *Computational Geosciences*, vol. 1, no. 1, pp. 1–33, 1997.
- [47] G. Cohen, *Higher-order Numerical Methods for Transient Wave Equations*, Springer-Verlag, 2002.
- [48] J. Tuomela, "A note on high order schemes for the one dimensional wave equation," *BIT Num. Math.*, vol. 35, no. 3, pp. 394–405, 1995.
- [49] G. Shubin and J. Bell, "A modified equation approach to constructing fourth order methods for acoustic wave propagation," *SIAM J. Scientific and Statistical Computing*, vol. 8, no. 2, pp. 135–151, 1987.
- [50] J. Tuomela, "On the construction of arbitrary order schemes for the many dimensional wave equation," *BIT Num. Math.*, vol. 36, no. 1, pp. 158–165, 1996.
- [51] S. Bilbao and B. Hamilton, "Construction and optimization techniques for high order schemes for the two-dimensional wave equation," in *Proc. Int. Cong. Acoustics (ICA)*, Montréal, Canada, 2013.
- [52] B. Hamilton and S. Bilbao, "Fourth-order and optimised finite difference schemes for the 2-D wave equation," in *Proc. Digital Audio Effects (DAFx)*, Maynooth, Ireland, 2013, pp. 146–153.
- [53] M. van Walstijn and K. Kowalczyk, "On the numerical solution of the 2D wave equation with compact FDTD schemes," in *Proc. Digital Audio Effects (DAFx)*, Espoo, Finland, 2008, pp. 205–212.
- [54] P. M. Morse and K. U. Ingard, *Theoretical Acoustics*, Princeton University Press, 1968.
- [55] G. Barton, *Elements of Green's Functions and Propagation: Potentials, Diffusion, and Waves*, Oxford University Press, 1989.
- [56] B. Hamilton and S. Bilbao, "Optimised 25-point finite difference schemes for the three-dimensional wave equation," in *Proc. Int. Cong. Acoustics (ICA)*, Buenos Aires, Argentina, Sept. 2016.

- [57] B. Hamilton, *Finite Difference and Finite Volume Methods for Wave-based Modelling of Room Acoustics*, Ph.D. thesis, University of Edinburgh, 2016.
- [58] F. Fontana, E. Bozzo, and M. Novello, "Decimation in time and space of finite-difference time-domain schemes: Standard isotropic lossless model," *IEEE Trans. Sig. Proc.*, vol. 63, no. 20, pp. 5331–5341, 2015.
- [59] J. Botts and L. Savioja, "Spectral and pseudospectral properties of finite difference models used in audio and room acoustics," *IEEE/ACM TASLP*, vol. 22, no. 9, pp. 1403–1412, Sept 2014.
- [60] N. Raghuvanshi, R. Narain, and M. C. Lin, "Efficient and accurate sound propagation using adaptive rectangular decomposition," *IEEE Trans. Vis. and CG*, vol. 15, no. 5, pp. 789–801, 2009.
- [61] S. Bilbao, "Modeling of complex geometries and boundary conditions in finite difference/finite volume time domain room acoustics simulation," *IEEE TASLP*, vol. 21, no. 7, pp. 1524–1533, July 2013.



Brian Hamilton received B.Eng. (Hons) and M.Eng. degrees in electrical engineering from McGill University in Montréal, QC, Canada, in 2009 and 2012, respectively, and his Ph.D. from the University of Edinburgh in 2016, as part of the NESS project (Next Generation Sound Synthesis), funded by the European Research Council (ERC). He is currently a Postdoctoral Research Fellow in the Acoustics and Audio Group at the University of Edinburgh, as part of the ERC-funded project WRAM (Wave-based Room Acoustic Modelling). His research interests

include numerical methods for 3-D room acoustics simulations and spatial audio.



Stefan Bilbao (B.A. Physics, Harvard, 1992, MSc., PhD Electrical Engineering, Stanford, 1996 and 2001 respectively) is currently Professor of Acoustics and Audio Signal Processing in the Acoustics and Audio Group at the University of Edinburgh, and was previously a lecturer at the Sonic Arts Research Centre, at the Queen's University Belfast, and a research associate at the Stanford Space Telecommunications and Radioscience Laboratories. He led the NESS project (Next Generation Sound Synthesis), funded by the European Research Council (ERC), run jointly

between the Acoustics and Audio Group and the Edinburgh Parallel Computing Centre at the University of Edinburgh between 2012 and 2016, and is currently PI on the ERC-funded project WRAM (Wave-based Room Acoustic Modelling).